

# Tailoring Electrode–Electrolyte Interfaces in Lithium-Ion Batteries Using Molecularly Engineered Functional Polymers

Laisuo Su, Jamie L. Weaver, Mitchell Groenenboom, Nathan Nakamura, Eric Rus, Priyanka Anand, Shikhar Krishn Jha, John S. Okasinski, Joseph A. Dura, and B. Reeja-Jayan\*



Cite This: *ACS Appl. Mater. Interfaces* 2021, 13, 9919–9931



Read Online

ACCESS |



Metrics & More



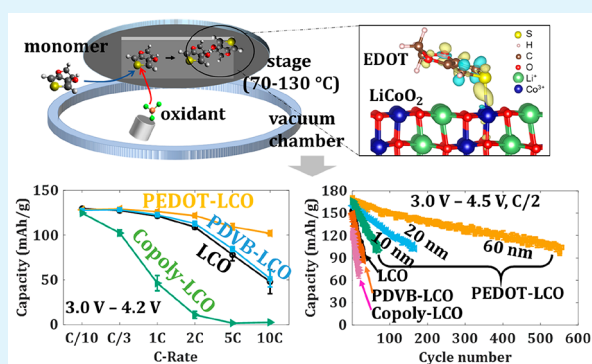
Article Recommendations



Supporting Information

**ABSTRACT:** Electrode–electrolyte interfaces (EIs) affect the rate capability, cycling stability, and thermal safety of lithium-ion batteries (LIBs). Designing stable EIs with fast  $\text{Li}^+$  transport is crucial for developing advanced LIBs. Here, we study  $\text{Li}^+$  kinetics at EIs tailored by three nanoscale polymer thin films via chemical vapor deposition (CVD) polymerization. Small binding energy with  $\text{Li}^+$  and the presence of sufficient binding sites for  $\text{Li}^+$  allow poly(3,4-ethylenedioxythiophene) (PEDOT) based artificial coatings to enable fast charging of  $\text{LiCoO}_2$ . Operando synchrotron X-ray diffraction experiments suggest that the superior  $\text{Li}^+$  transport property in PEDOT further improves current homogeneity in the  $\text{LiCoO}_2$  electrode during cycling. PEDOT also forms chemical bonds with  $\text{LiCoO}_2$ , which reduces Co dissolution and inhibits electrolyte decomposition. As a result, the  $\text{LiCoO}_2$  4.5 V cycle life tested at C/2 increases over 1700% after PEDOT coating. In comparison, the other two polymer coatings show undesirable effects on  $\text{LiCoO}_2$  performance. These insights provide us with rules for selecting/designing polymers to engineer EIs in advanced LIBs.

**KEYWORDS:** lithium-ion batteries, electrode–electrolyte interface, surface engineering,  $\text{LiCoO}_2$ , chemical vapor deposition polymerization, poly(3,4-ethylenedioxythiophene), synchrotron X-ray characterization, density functional theory calculation



## INTRODUCTION

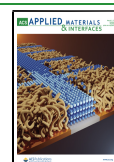
The electrode–electrolyte interface (EEI) is recognized as one of the most crucial components inside lithium-ion batteries (LIBs) because of the diverse phenomena that occur in this region: charge transfer reactions, electrolyte decomposition, and electrode (cathode, anode) degradation.<sup>1</sup> Engineering the EEI with the desired properties is important for developing advanced LIBs with high power densities, a high degree of thermal safety, and long lifespans.<sup>2–5</sup> Although many artificial coatings (organic and inorganic) have been applied to engineer the EEI, we currently have a limited understanding of the  $\text{Li}^+$  kinetics in these artificial coatings and at the EEI.<sup>6</sup> For example, Li et al. reported that  $\text{Li}^+$  migration at the EEI mediates phase transformation in cathode particles of  $\text{LiFePO}_4$ . They proposed that engineering the EEI with coatings can change the in-plane  $\text{Li}^+$  migration, thereby controlling the electrochemical performance of  $\text{LiFePO}_4$ .<sup>3</sup> However, this hypothesis has not been validated. The difficulty to study  $\text{Li}^+$  kinetics in LIBs was also highlighted by Xu. et al., where they stressed the importance of experimentally measuring  $\text{Li}^+$  ion conductivity and mobility in artificial coatings.<sup>7</sup> Therefore, further investigations are needed to uncover the  $\text{Li}^+$  transport in artificial coatings and at EEI for developing advanced LIBs.

The systematic investigation of  $\text{Li}^+$  kinetics in artificial coatings requires techniques that can grow uniform and conformal nanoscale layers with a controllable thickness. Thus far, the majority of coating methods are based on wet chemical processes such as sol–gel synthesis, hydro/solvothermal synthesis, and chemical polymerization.<sup>8</sup> These techniques incorporate both organic and inorganic materials, but they suffer from surface tension and dewetting effects that lead to nonuniform film thickness and nonconformal surface coverage.<sup>8</sup> In parallel, deposition techniques have been developed to alleviate these issues, including chemical vapor deposition (CVD) and atomic layer deposition.<sup>9</sup> Recently, our group introduced a novel low-temperature CVD polymerization technique to engineer uniform polymer artificial coatings on battery electrodes.<sup>2</sup> Here, we use this low-temperature CVD process to synthesize nanoscale polymer coatings on  $\text{LiCoO}_2$  electrodes with precise control over the thickness and

Received: November 24, 2020

Accepted: February 10, 2021

Published: February 22, 2021



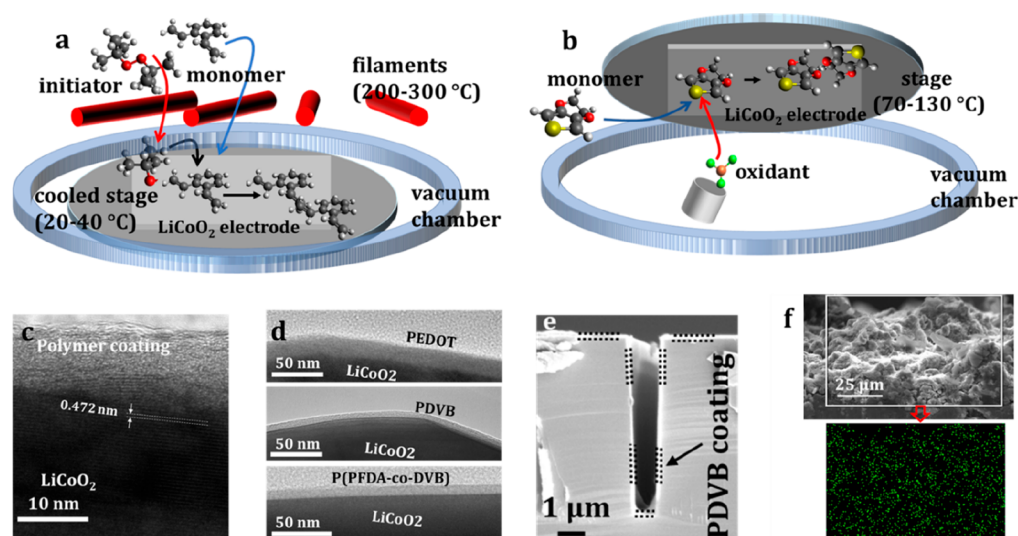


**Figure 1.** Chemical vapor deposition (CVD) polymerization techniques and characterization of polymer coatings on different substrates. (a, b) Schematics of initiated CVD (iCVD) polymerization (a) and oxidative CVD (oCVD) polymerization (b). These two CVD systems can deposit polymer thin films on casted electrodes by a one-step process. (c, d) High-resolution TEM images show 10–20 nm thick polymer thin films are uniformly deposited on the surface of  $\text{LiCoO}_2$  particles via the CVD polymerization techniques. The 0.472 nm shows the (003)  $d$  spacing in  $\text{LiCoO}_2$ . (e) SEM image shows that the CVD technique can engineer uniform coatings on nonplanar structures (like a silicon trench). Such conformal coatings cannot be realized by solution-based methods due to surface tension and dewetting effects. (f) EDS mapping of sulfur (S) along the cross-section of a  $\text{LiCoO}_2$  electrode, where S is continuously distributed along the selected area.

conformal surface coverage. Specifically, we examined three CVD synthesized polymers as artificial coatings. Poly(3,4-ethylenedioxythiophene) (PEDOT), poly(divinylbenzene) (PDVB), and poly(1H,1H,2H,2H-perfluorodecyl acrylate-*co*-divinylbenzene) (P(PFDA-*co*-DVB) or copolymer) were selected because of their good mechanical stability and high melting points.<sup>10</sup> The nanoscale engineering capability of CVD polymerization is critical for investigating the relationships between polymer structure, composition and  $\text{Li}^+$  kinetics, and resultant electrode behavior.<sup>10</sup> Furthermore, more than 50 different polymer chemistries have been successfully synthesized via CVD polymerization techniques, and this chemical diversity provides a large space of unexplored materials for engineering EEIs.<sup>10–12</sup>

Electrochemical impedance spectroscopy (EIS) can investigate the kinetics of  $\text{Li}^+$  at EEI in LIBs because it can resolve different transport processes based on their time constants by measuring impedance at different frequencies.<sup>13</sup> However, processes with similar time constants are coupled in EIS and cannot be resolved, such as  $\text{Li}^+$  desolvation process and charge transfer process.<sup>14</sup> To fully uncover  $\text{Li}^+$  kinetics at EEI and in artificial coatings, we combine experimental tools like neutron reflectometry and depth profiling to investigate the properties (such as thickness, density) of nanoscale CVD grown polymer coatings, as well as to understand  $\text{Li}^+$  transport in these polymers. Density functional theory (DFT) calculations determine the interaction between  $\text{Li}^+$  and CVD polymers, enabling comparison of the  $\text{Li}^+$  binding energy and the number of  $\text{Li}^+$  binding sites available in these polymers. Synchrotron operando energy dispersive X-ray diffraction (ED-XRD) is further used to investigate the effect of  $\text{Li}^+$  kinetics on  $\text{LiCoO}_2$  phase transition during cycling. This combination of experimental and computational techniques reveals that the PEDOT coating demonstrates enhanced  $\text{Li}^+$  kinetics, leading to increased current homogeneity in the  $\text{LiCoO}_2$  electrodes and consequently improved rate capability of  $\text{LiCoO}_2$  cells. In

comparison, the other two polymer coatings (PDVB and P(PFDA-*co*-DVB)) both show poor  $\text{Li}^+$  kinetics, resulting in low rate capability of  $\text{LiCoO}_2$  electrodes. Furthermore, we find that the PEDOT coating can form chemical bonds with Co in  $\text{LiCoO}_2$ , increasing the 4.5 V cycle life by over 1700%. On the basis of these fundamental insights, we propose design rules for selecting and designing polymer coatings to engineer EEIs for advanced LIBs.

## RESULTS AND DISCUSSION

**Engineering  $\text{LiCoO}_2$  Surface Using CVD Polymerization.** The  $\text{LiCoO}_2$  powder selected for this study contains micron-sized secondary particles that are composed of primary particles with 2.1  $\mu\text{m}$  (average) diameter (Figure S1a of the Supporting Information, SI). The powder shows the expected hexagonal unit cell with a space group of  $R\bar{3}m$  (Figure S1b). Cast  $\text{LiCoO}_2$  electrodes, rather than the active material powder, were utilized for the surface engineering during initiated CVD (iCVD) and oxidative CVD (oCVD) polymer deposition processes. Table S1 displays the experimental conditions for synthesizing polymers. During the iCVD synthesis, the monomer and initiator were vaporized and introduced into a vacuum reactor with controllable flow rates. The labile initiator was thermally cleaved using resistively heated nichrome filaments, generating radicals that attacked monomer molecules adsorbed on  $\text{LiCoO}_2$  electrodes and triggered free-radical polymerization. During the oCVD synthesis, the monomer was introduced into a vacuum reactor and adsorbed on the surface of  $\text{LiCoO}_2$  electrodes.  $\text{FeCl}_3$  oxidant was then sublimed and spontaneously reacted with the monomer vapors, resulting in thin-film growth on  $\text{LiCoO}_2$  electrodes. The schematics for synthesizing PEDOT, PDVB, and P(PFDA-*co*-DVB) are illustrated in Table S1.

Figure 1a,b shows the two CVD deposition processes. Details for the synthesis of PEDOT and PDVB polymers via CVD polymerization techniques can be found in our previous

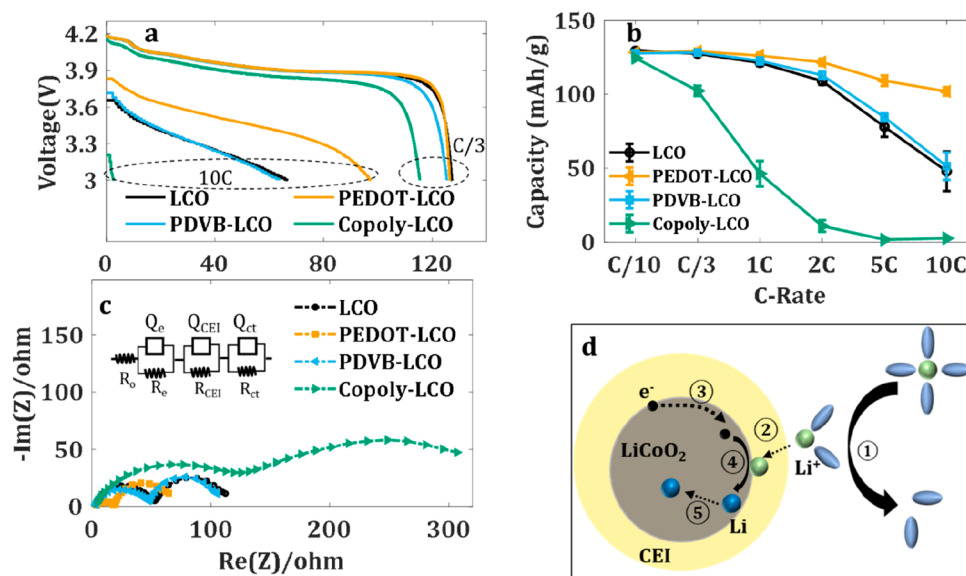


**Figure 2.** Influence of 10 nm polymer coatings on the kinetics of LiCoO<sub>2</sub> electrodes. (a) Discharge curves at C/3 and 10C for the four investigated LiCoO<sub>2</sub> electrodes, where 1C = 145 mA/g. (b) Statistical comparison of cell capacities tested at 3.0–4.2 V. Four samples were measured in each case. (c) The effect of polymer coatings on the electrochemical impedance of the LiCoO<sub>2</sub> electrode measured at 20 °C. Inset shows an ECM used for fitting. (d) A schematic illustration for the Li<sup>+</sup> transport process from the electrolyte to a LiCoO<sub>2</sub> particle, including ① Li<sup>+</sup> desolvation process, ② Li<sup>+</sup> diffusion within CEI, ③ e<sup>-</sup> transport in LiCoO<sub>2</sub>, ④ Li<sup>+</sup> combination with e<sup>-</sup> to form Li<sup>+</sup>-e<sup>-</sup> pair, and ⑤ Li<sup>+</sup>-e<sup>-</sup> pair diffusion in the LiCoO<sub>2</sub> particle.

work.<sup>2</sup> X-ray photoelectron spectroscopy (XPS) was applied to study the composition of PEDOT and P(PFDA-*co*-DVB). Approximately 25% (by moles) of the PEDOT film is doped with Cl from the FeCl<sub>3</sub> oxidant, which balances the positive charge in the PEDOT chain (Figure S2a).<sup>15,16</sup> The copolymer sample consists of ~39% PFDA and ~61% DVB (by moles) (Figure S2b,c).<sup>17</sup> It needs to be noted that the XPS technique only captures the near-surface region. The composition of polymers in bulk could be different compared to the near-surface region.

The initiator to monomer ratio used in CVD polymerization is generally much higher than that used in traditional solution-based polymerization techniques, leading to different polymer properties like molecular weight and polymer density.<sup>10</sup> However, there are limited measurements reported for the density of CVD synthesized polymer films because of the difficulty in measuring nanoscale-thick films. Here, we use neutron reflectometry (NR) to measure the densities of CVD synthesized nanoscale polymer thin films. The results are included in Figure S3 and Table S2. The densities of the CVD synthesized PEDOT and PDVB are similar to the values reported in the literature (Table S3).<sup>18,19</sup> Small discrepancies could be from differences in synthesis tools and conditions. These density values are essential to understand the interactions between CVD synthesized polymers and Li<sup>+</sup> that we explore in this work. Neutron depth profiling (NDP) was applied to examine the possible uptake of Li<sup>+</sup> in the three CVD-grown polymers under static conditions. The details of the experimental process and the NDP data are shown in Figure S4. The NDP profiles for the three polymers indicate no statistically significant uptake of Li into the thin films during the soaking process.

The polymer-coated LiCoO<sub>2</sub> electrodes were characterized by transmission electron microscopy (TEM) and scanning electron microscopy (SEM). Figure 1c shows a 10 nm thick CVD polymer layer parallel to the (003) plane of a LiCoO<sub>2</sub>

particle, suggesting the polymer is successfully coated on the particle by CVD polymerization. Larger regions of LiCoO<sub>2</sub> particles seen in Figure 1d show that all three polymers conformally cover the surface of the particles. Cross-section SEM and energy-dispersive X-ray spectroscopy (EDS) elemental mapping were applied to examine the effectiveness of the CVD polymerization technique to engineer coatings on nonplanar structures.<sup>20</sup> Figure 1e shows that ~100 nm thick PDVB is uniformly coated on the surface of a silicon trench. The coating is conformal with a constant thickness along the edge, suggesting that CVD polymerization allows the monomer and initiator molecular to penetrate into porous electrode layers and effectively shrink-wrap electrode particles. Precisely engineering such a conformal coating is impossible by solution-based methods due to surface tension and dewetting effects.<sup>10</sup> Figure 1f displays the distribution of sulfur (S) along the cross-section of a PEDOT-coated LiCoO<sub>2</sub> electrode prepared by doctor blading. As S is only expected to be present in PEDOT, the continuous distribution of S along the cross-section indicates that the PEDOT polymer covers the whole electrode, rather than only the exterior face of the electrode. It must be mentioned that obtaining a conformal polymer coating on LiCoO<sub>2</sub> electrodes is not trivial. Various experiment parameters, such as temperature, chamber pressure, and precursors flow rate, need to be precisely controlled, as described in the Experimental Section.

**Kinetics of Li<sup>+</sup> in Pristine and Polymer-Coated LiCoO<sub>2</sub> Electrodes.** By building a polymer nanolayer on a LiCoO<sub>2</sub> electrode, we change the composition of the cathode-electrolyte-interphase (CEI). This alters the transport of electrons within LiCoO<sub>2</sub> particles as well as the transport of Li<sup>+</sup> between the electrolyte and the electrode, thereby affecting the rate capability of the LiCoO<sub>2</sub> electrode. To investigate the effect of the polymer coatings on the rate capability of the LiCoO<sub>2</sub> electrode, we tested coin cells at six different C-rates, including C/10, C/3, 1C, 2C, 5C, and 10C, as shown in Figure

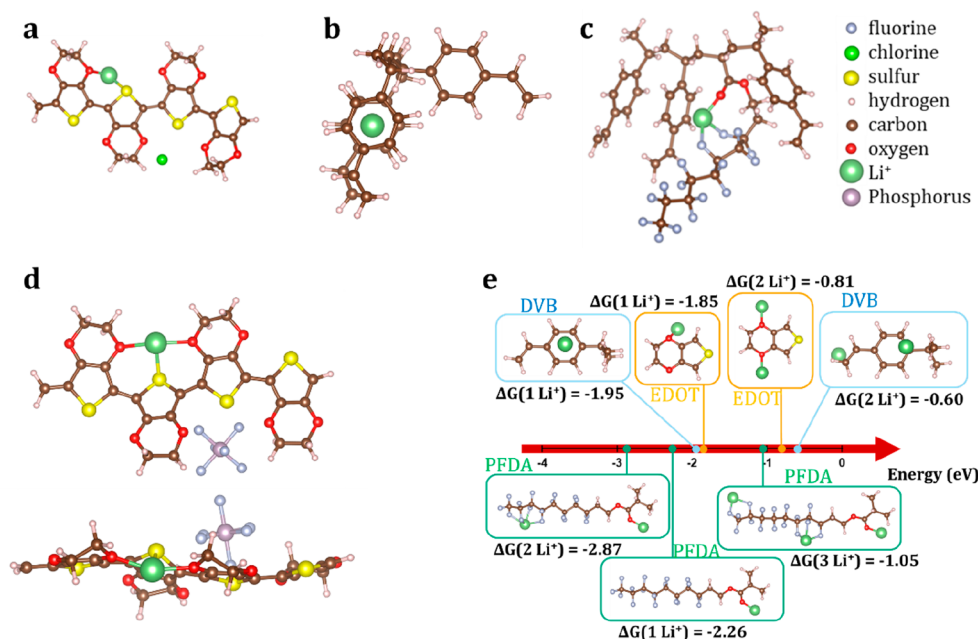


**Figure 3.** Density functional theory (DFT) calculations of the interactions between  $\text{Li}^+$  and different polymers. (a–d) The interaction between  $\text{Li}^+$  and PEDOT (Cl doped) (a), PDVB (b), P(PFDA-co-DVB) (c), and PEDOT ( $\text{PF}_6^-$  doped) (d). The formation energy is  $-2.17$ ,  $-3.15$ ,  $-3.92$ , and  $-2.21$  eV for system a, b, c, and d, respectively. Polymers with four repeating units are used for DFT calculation to avoid unaffordable calculation cost. (e) Cumulative binding energy between  $\text{Li}^+$  and different polymer repeating units (monomers). Each monomer can bind at most 2, 2, and 3  $\text{Li}^+$  for DVB, EDOT, and PFDA, respectively. Small binding energy with  $\text{Li}^+$  and the presence of ample binding sites for  $\text{Li}^+$  make PEDOT a favorable  $\text{Li}^+$  conductor compared to PDVB and P(PFDA-co-DVB) (Table S5).

SS. Figure 2a compares the discharge curves of the  $\text{LiCoO}_2$  electrodes tested at C/3 and 10C, where 1C = 145 mA/g. The discharge curves of the PDVB-coated  $\text{LiCoO}_2$  and the pristine  $\text{LiCoO}_2$  almost overlap each other at the two C-rates, suggesting the negligible effect of the PDVB coating on the rate performance of the  $\text{LiCoO}_2$  electrode. In comparison, the PEDOT-coated  $\text{LiCoO}_2$  shows a higher capacity and lower overpotential at 10C. The specific capacity is increased from 60 mA h/g to 99 mA h/g, and the middle voltage is increased from 3.30 to 3.48 V. Thus, the PEDOT coating improves the rate performance of the  $\text{LiCoO}_2$  electrode. In contrast, the copolymer-coated  $\text{LiCoO}_2$  shows a smaller capacity and larger overpotential at both C/3 and 10C, indicating that the copolymer reduces the rate performance of the  $\text{LiCoO}_2$ .

Figure 2b summarizes the rate capacities of different  $\text{LiCoO}_2$  electrodes. The result indicates that the specific capacities at high rates ( $>5\text{C}$ ) are much higher in the PEDOT-coated  $\text{LiCoO}_2$  than that in the pristine  $\text{LiCoO}_2$ . For example, the average 10C capacity is increased from 48 mA h/g to 102 mA h/g by introducing a 10 nm thick PEDOT coating. In comparison, the copolymer coating largely decreases the rate capability, while the PDVB coating has no significant effect. EIS was conducted to investigate the effect of different polymer coatings on the kinetics of  $\text{Li}^+$  and electrons in  $\text{LiCoO}_2$  electrodes. Figure 2c compares the impedance of coin cells with different  $\text{LiCoO}_2$  electrodes. As the same Li metal was used as the anode for all tested coin cells, the different impedance was contributed from the cathode side. The result suggests that the PEDOT coating reduces the overall impedance of the electrode, while the copolymer coating increases the impedance and the PDVB coating has no significant effect. The impedance result matches well with the rate capability shown in Figure 2a,b.

Figure 2d decouples the transport process of a  $\text{Li}^+$  from electrolytes to a  $\text{LiCoO}_2$  particle that can be divided into five steps. Step ① is the desolvation process of  $\text{Li}^+$  to get rid of bulky solvent; Step ② is the transport of  $\text{Li}^+$  in CEI; Step ③ is the transport of electron in/on  $\text{LiCoO}_2$  particles; and Step ④ is the combination of  $\text{Li}^+$  and electron to form  $\text{Li}^+ \cdot e^-$  pair. The final step ⑤ is the transport of the  $\text{Li}^+ \cdot e^-$  pair into the  $\text{LiCoO}_2$  particle. The transport steps ①–④ are all affected by polymer coatings, leading to different kinetics of the  $\text{LiCoO}_2$  electrodes. Some steps can be decoupled from the EIS results because of their different time constants.<sup>21,22</sup> For example, step ② is represented as the semicircle at the high-middle frequency in the EIS data ( $R_{\text{CEI}}$ ). Step ① and ④ are represented as the semicircle at the middle-low frequency in the EIS data ( $R_{\text{ct}}$ ).

To uncover the effect of polymer coatings on the kinetics of  $\text{LiCoO}_2$  electrodes, we measured the impedance of the electrodes at four temperatures, including  $-15$  °C,  $0$  °C,  $15$  °C, and  $30$  °C. A third-order equivalent circuit model (ECM) was applied to fit the measured data, and the results are shown in Figure S6. The PEDOT-coated electrode shows the smallest impedance at all the measured temperatures among the three polymer-coated  $\text{LiCoO}_2$  electrodes. The reduced  $R_{\text{CEI}}$  and  $R_{\text{ct}}$  from the PEDOT coating are related to the interaction between  $\text{Li}^+$  and the polymer, which will be discussed in the next section on DFT calculations. Additionally, the change in  $R_{\text{CEI}}$  and  $R_{\text{ct}}$  with respect to temperature follows the Arrhenius equation (eq 1.) This agrees with the fact that they are attributed to electrochemical processes.<sup>23</sup> Table S4 lists the calculated activation energy ( $E_a$ ) and the pre-exponential factor ( $A$ ) for  $R_{\text{CEI}}$  and  $R_{\text{ct}}$  based on eq 1. Interestingly, the  $A$  value of the PEDOT-coated electrode is 2 to 3 orders of magnitude higher than that in the other two polymer-coated  $\text{LiCoO}_2$  electrodes. As the pre-exponential factor is proportional to the attempt frequency, a high  $A$  value in the PEDOT-coated

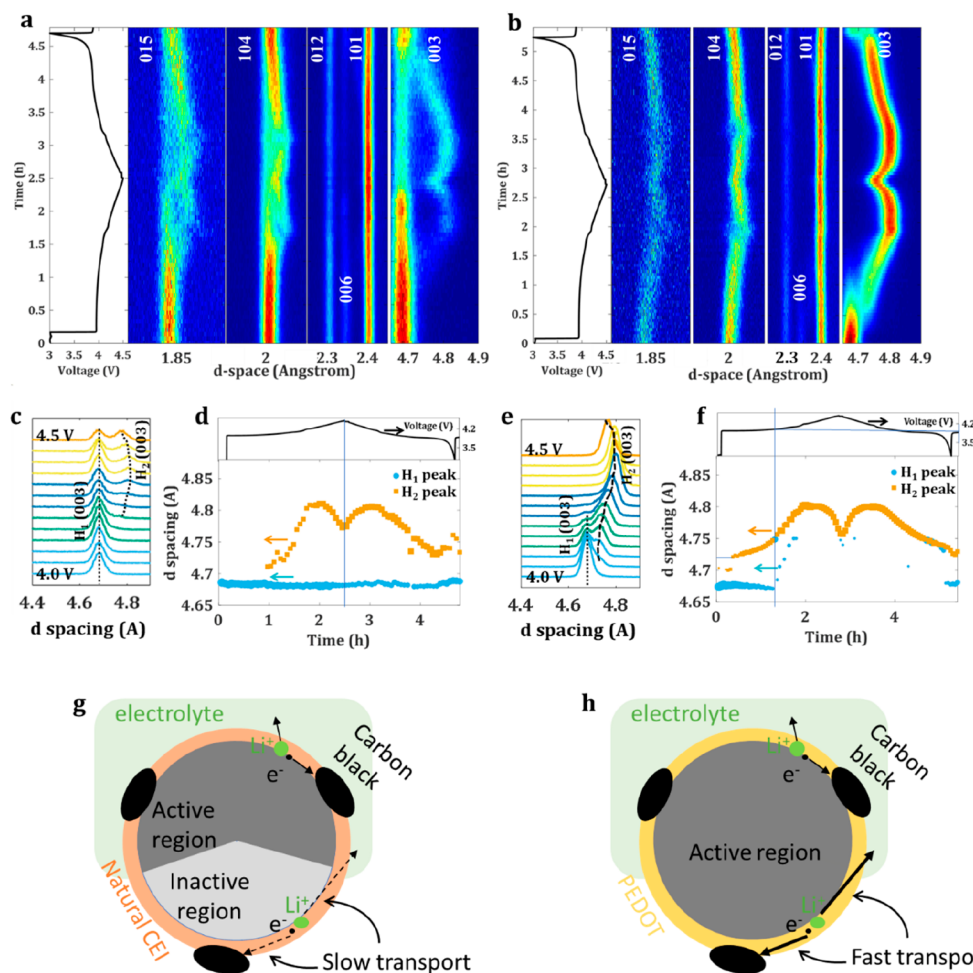


**Figure 4.** Synchrotron operando ED-XRD evidence for the improved current homogeneity in LiCoO<sub>2</sub> electrodes after the PEDOT coating. (a, b) The voltage profiles and the corresponding contour plots showing XRD peak evolution for a pristine LiCoO<sub>2</sub> electrode (a) and a 10 nm PEDOT-coated LiCoO<sub>2</sub> electrode (b) during one cycle at C/2 with a cutoff voltage at 4.5 V. The intensity of a peak is represented by different colors, with blue indicating lower intensity and red indicating higher intensity. (c, e) Selected ED-XRD patterns of the pristine LiCoO<sub>2</sub> (c) and the PEDOT-coated LiCoO<sub>2</sub> electrode (e), with peak shifts denoted by the dashed black curves. (d, f) The evolution of *d*-spacing in (003) peak during cycling. The marker size represents the intensity of the corresponding peak. The arrows point to the axis for different curves. (g, h) Schematics show the effect of PEDOT coating on the current homogeneity in LiCoO<sub>2</sub> electrodes during cycling. The PEDOT coating provides fast transport channels for both Li<sup>+</sup> and electrons, making regions with poor contact to electrolyte or carbon black active during cycling.

electrode suggests that the PEDOT polymer thin film can take in more Li<sup>+</sup> from electrolyte under the electric field than the other two polymers.

$$\frac{1}{R_{\Omega}} = A \times \exp\left(-\frac{E_a}{RT}\right) \quad (1)$$

where  $R_{\Omega}$  is the resistance,  $A$  is the pre-exponential factor, which is a constant,  $E_a$  the activation energy,  $R$  the universal gas constant, and  $T$  is the temperature.

#### DFT Calculations for Li<sup>+</sup> Kinetics in Polymer Coatings.

Li<sup>+</sup> transport in the three polymers follows rules of ionic transport in glassy materials because of their relatively high melting points.<sup>24</sup> Li<sup>+</sup> movement depends on the activation energy of Li<sup>+</sup> hopping from one site to another, driven by the concentration gradient of Li<sup>+</sup> and the externally applied electric field, giving collective movement on a macroscopic scale. However, it is difficult to calculate the hopping activation energy through DFT simulation because most polymers, like PDVB, are amorphous. Even if a polymer has some degree of crystallinity, like PEDOT, extended polymer matrices are too

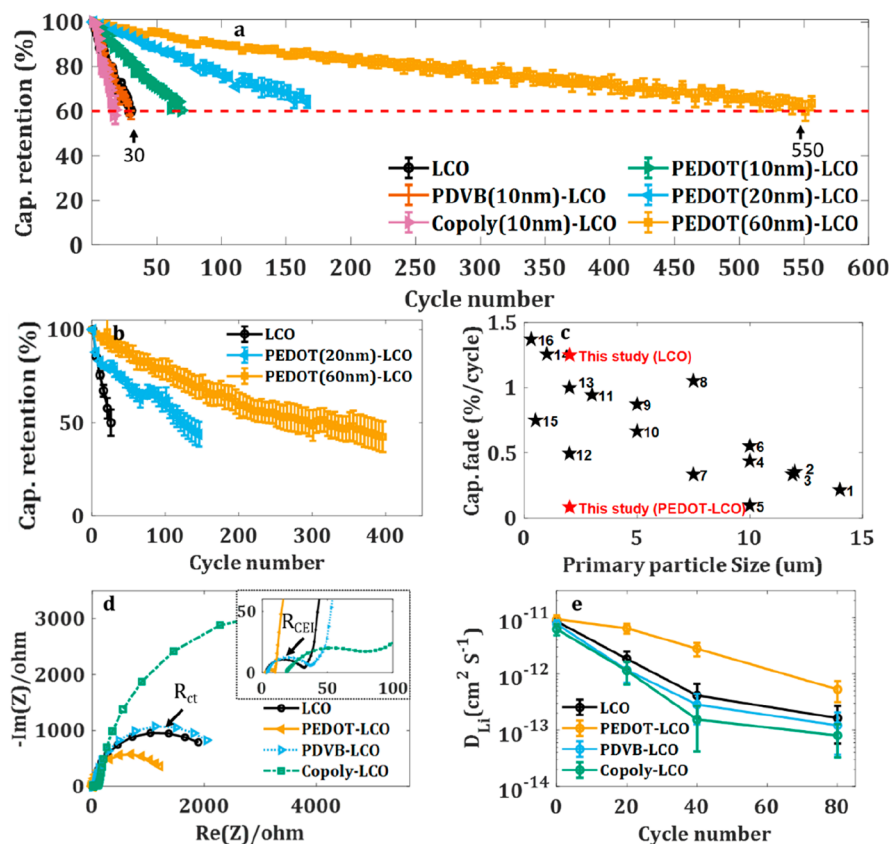
large to be simulated with nonperiodic DFT.<sup>25</sup> To solve this problem, we calculated two alternative descriptors that relate to the hopping activation energy, which are the binding energy between Li<sup>+</sup> and a small polymer cluster and the number of Li<sup>+</sup> binding sites present in a polymer.

Figure 3 shows the DFT calculation results of the interactions between Li<sup>+</sup> and different polymers using eq 2. Figure 3a–c shows the lowest energy configurations when one Li<sup>+</sup> is added to the polymer matrix. The binding energy between Li<sup>+</sup> and PEDOT, PDVB, and copolymer is –2.17, –3.15, and –3.92 eV, respectively. The relatively weak binding energy between Li<sup>+</sup> and PEDOT could be one reason for good Li<sup>+</sup> kinetics in the PEDOT-coated LiCoO<sub>2</sub>.

$$\Delta G_{\text{bind}} = G(\text{polymer} + \text{Li}^+) - G(\text{polymer}) - G(\text{Li}^+) \quad (2)$$

where  $\Delta G_{\text{bind}}$  is the binding energy between a polymer and Li<sup>+</sup>;  $G(x)$  the Gibbs free energy of the  $x$  system in a vacuum, and  $x$  stands for a structure, including polymer, Li<sup>+</sup>, or polymer + Li<sup>+</sup>.

Since LiPF<sub>6</sub>-based electrolytes were utilized in LIBs, PF<sub>6</sub><sup>–</sup> could replace Cl<sup>–</sup> in oCVD PEDOT.<sup>25</sup> Figure 3d shows that



**Figure 5.** Comparing LiCoO<sub>2</sub> electrodes 4.5 V cycle life performance after polymer coatings. (a) The capacity retention of different LiCoO<sub>2</sub> electrodes tested at C/2 in the voltage range of 3.0–4.5 V. (b) The capacity retention of different LiCoO<sub>2</sub> electrodes tested at 5C in the voltage range of 3.0–4.5 V. (c) Comparison of 4.5 V high voltage cycling performance of LiCoO<sub>2</sub> with different particle sizes. Data is collected from recently published papers, as listed in Table S6. LiCoO<sub>2</sub> electrodes 4.5 V cycle life increases (by around 1700%) after PEDOT coating in this study. (d) Comparison of EIS for different types of LiCoO<sub>2</sub> electrodes after 60 cycles. The polymer thicknesses are 10 nm. Inset shows  $R_{CEI}$ . (e) The evolution of Li apparent diffusion coefficient in different LiCoO<sub>2</sub> electrodes measured using GITT. The values are averaged for all measured  $D_{Li}$  values between 4.0 and 4.5 V.

the dopant exchange from  $Cl^-$  to  $PF_6^-$  has little effect on the binding energy between PEDOT and  $Li^+$  (from  $-2.17$  eV to  $-2.21$  eV). We also studied the effect of  $PF_6^-$  on  $Li^+$  transport in PDVB and P(PFDA-co-DVB) by calculating the binding energy between  $PF_6^-$  and these polymers. The calculated results in Figure S7 show that the binding energy between  $PF_6^-$  and PDVB/P(PFDA-co-DVB) is relatively small, suggesting the interaction between them could be ignored when studying the interaction between  $Li^+$  and these polymers. Additionally, when both  $Li^+$  and  $PF_6^-$  are considered in PDVB and P(PFDA-co-DVB) systems, no minimum energy stationary points could be found that do not result in a Li- $PF_6$  ion pair, which further limits the transport of  $Li^+$  in the two polymers.

The number of  $Li^+$  binding sites in polymers was studied by calculating the cumulative binding energy between  $Li^+$  and monomers as well as small polymer clusters. Figure 3e shows that each EDOT monomer and DVB monomer can provide two binding sites for  $Li^+$ , while each PFDA monomer can provide three sites. By considering the molecular weight of the monomer and the density of the polymer thin film (Table S3), we calculated the concentration of  $Li^+$  binding sites in different polymers (Table S5). The results suggest that PEDOT has the highest number of  $Li^+$  binding sites available, followed by PDVB and P(PFDA-co-DVB). Indeed, PEDOT provides almost twice as many  $Li^+$  binding sites compared to the copolymer. These results agree well with the much larger pre-

exponential factor value of the PEDOT-coated electrode (Table S4). Small binding energy with  $Li^+$  and the presence of ample binding sites for  $Li^+$  make PEDOT a significantly better  $Li^+$  conductor compared to PDVB and P(PFDA-co-DVB). This can also explain the smaller  $R_{CEI}$  and  $R_{ct}$  in the PEDOT-coated LiCoO<sub>2</sub> compared to the other two polymer-coated LiCoO<sub>2</sub> electrodes (Figure 2c).

**Synchrotron Operando ED-XRD Characterization of LiCoO<sub>2</sub>.** As PEDOT coating promotes the transport of both electrons and  $Li^+$  at EELs, it can potentially improve current homogeneity in LiCoO<sub>2</sub> electrodes, especially at high C-rates. To investigate the current homogeneity, synchrotron operando ED-XRD was applied to monitor the evolution of LiCoO<sub>2</sub> crystal structure during cycling. Generally,  $Li_xCoO_2$  ( $0 \leq x \leq 1$ ) goes through a metal–insulator transition between two hexagonal phases ( $H_1$  to  $H_2$ ) when  $x$  decreases from 0.95 to 0.75, and the  $H_2$  phase has a larger  $c$  parameter than the  $H_1$  phase.<sup>26,27</sup> Beyond  $x < 0.75$ , the  $H_1$  phase disappears, resulting in a single-phase region with only the  $H_2$  phase and an increasing  $c$  lattice parameter. At around  $x = 0.5$ , the  $Li_xCoO_2$  goes through an order–disorder transition, where there is a phase transformation from hexagonal to monoclinic and then back to hexagonal, and the  $c$  parameter of the  $H_2$  phase reaches its maximum. Keeping delithiation under  $x < 0.5$  induces a dramatic decrease of the  $c$  parameter of the  $H_2$  phase.<sup>27</sup>

Figure 4 compares the ED-XRD results for a pristine LiCoO<sub>2</sub> electrode and a PEDOT-coated LiCoO<sub>2</sub> electrode cycled at C/2. The electrochemical cycling curves in Figure 4a,b shows the first charge–discharge cycle of the two electrodes tested within the voltage range of 3.0–4.5 V. The specific discharge capacity of the PEDOT-coated LiCoO<sub>2</sub> (177 mA h/g) is higher than that of the pristine LiCoO<sub>2</sub> (153 mA h/g). In addition, Figure S8a indicates that the PEDOT coating reduces the cell overpotential during the charge and discharge process. The two-dimensional contour plots in Figure 4a,b show the structural evolutions of the two LiCoO<sub>2</sub> electrodes during cycling, which are quite different.

It needs to be mentioned that previous studies generally apply a very small C-rate, such as C/50, during the operando experiment.<sup>26</sup> The small C-rate allows the XRD information to be collected at the quasi-steady-state of the LiCoO<sub>2</sub> electrode. To study the Li<sup>+</sup> kinetics during cycling, we cycled cells at a relatively large C-rate (C/2) during the operando experiment, which could cause nonsteady state of the LiCoO<sub>2</sub> electrode and inhomogeneous Li distribution in the electrode.<sup>28</sup> For example, a pronounced nonsteady-state and inhomogeneous Li distribution occurs in the pristine LiCoO<sub>2</sub> electrode, as shown in Figure 4a. The structural evolution of the pristine LiCoO<sub>2</sub> significantly deviates from existing studies.<sup>26,27</sup> Figure 4c,d further highlights the evolution of the (003) peak. The second (003) peak appears after around 53.6 mA h/g of charging, corresponding to an average composition of Li<sub>0.80</sub>CoO<sub>2</sub>. In addition, the H<sub>1</sub> phase does not disappear during the whole cycling process, suggesting that the *x* value in some Li<sub>*x*</sub>CoO<sub>2</sub> particles does not go below 0.75 during cycling. The portion of inactive Li<sub>*x*</sub>CoO<sub>2</sub> is around 30% in the pristine LiCoO<sub>2</sub> electrode during cycling, as shown in Figure S8b. Thus, an abnormally large fraction of Li<sub>*x*</sub>CoO<sub>2</sub> particles are relatively inactive during the cycling test.

In comparison, all PEDOT-coated LiCoO<sub>2</sub> particles are active during cycling at C/2 (Figure 4b). The structural evolution of the PEDOT-coated LiCoO<sub>2</sub> matches well with existing studies on LiCoO<sub>2</sub> (Figure 4b).<sup>26,27</sup> Figure 4e,f highlights the evolution of the (003) peak in Figure 4b. The result shows that a second (003) peak appears after around 17.3 mA h/g of charging, suggesting the start of the phase transition from the H<sub>1</sub> phase to the H<sub>2</sub> phase. The average composition of the electrode is Li<sub>0.937</sub>CoO<sub>2</sub> at this point. When the charge capacity reaches 82.4 mA h/g, the H<sub>1</sub> peak disappears, indicating all the H<sub>1</sub> phase has transferred to the H<sub>2</sub> phase in the electrode. The average composition of the electrode at this point is Li<sub>0.7</sub>CoO<sub>2</sub>. The PEDOT-coated LiCoO<sub>2</sub> electrode compositions at the two critical points, where the H<sub>2</sub> phase appears, and the H<sub>1</sub> phase disappears, are close to that reported in the literature, which are Li<sub>0.95</sub>CoO<sub>2</sub> and Li<sub>0.75</sub>CoO<sub>2</sub>, respectively.

Figure 4g,h shows schematics to explain how PEDOT coating improves current homogeneity in LiCoO<sub>2</sub> electrodes. In pristine LiCoO<sub>2</sub>, some regions have poor contact with the electrolyte or the regions with conducting carbon black. These regions become inactive when the Li<sup>+</sup> and electrons transport speed cannot keep up with the cycling C-rates. In comparison, the PEDOT coating provides fast transport channels for both Li<sup>+</sup> and electrons and, thus, increases the amount of active region available during cycling. We tested ED-XRD at three different locations on both samples, and they all showed similar results (Figure S8). Therefore, the PEDOT coating improves the current homogeneity in the LiCoO<sub>2</sub> electrode by providing

fast transport channels for electrons and Li<sup>+</sup>. This could alleviate spatially heterogeneous deterioration of LiCoO<sub>2</sub> electrodes and, thus, improve their cycling stability.

**Effect of Polymer Coatings on LiCoO<sub>2</sub> Cycling Stability.** Figure 5a shows that a 10 nm thick PEDOT coating decreases the LiCoO<sub>2</sub> capacity fading rate (tested at C/2 within 3.0–4.5 V) from 1.33%/cycle to 0.57%/cycle, while the P(PFDA-*co*-DVB) with the same thickness increases the value to 2.22%/cycle and the PDVB shows no significant effect. By increasing the coating thickness of PEDOT to 60 nm, we further reduce the capacity fading rate from 1.33%/cycle to 0.073%/cycle, corresponding to over 1700% of cycle life improvement (see SI for details). This cycle life increase is significantly higher than values reported by existing studies that apply CVD polymers on battery cathodes, which only increase the cycle life of LiMn<sub>2</sub>O<sub>4</sub> by around 70%<sup>2</sup> and Li-Ni<sub>0.8</sub>Co<sub>0.1</sub>Mn<sub>0.1</sub>O<sub>2</sub> by around 500%.<sup>7</sup> The PEDOT coating not only increases LiCoO<sub>2</sub> discharge capacity from 153 mA h/g to 171 mA h/g (Figure S9a), but also significantly mitigates the voltage decay during cycling (Figure S9b,c). Better rate capability and improved cycling stability suggest that the PEDOT artificial coating has the potential to enable the fast charge of LiCoO<sub>2</sub> electrodes at high voltage. Figure 5b shows the cycling stability of LiCoO<sub>2</sub> electrodes at 5C. The result suggests that the cycle number is increased from 30 cycles to 300 cycles by applying a 60 nm thick PEDOT coating when the LiCoO<sub>2</sub> degrades to 50% of its initial capacity. The initial 5C discharge capacity is also increased from 104.8 to 132.3 mA h/g after PEDOT coating (Figure S9d). Figure S9e shows that the cycle life improvement is not significant when increasing the PEDOT thickness from 40 to 60 nm. Thus, we did not go beyond 60 nm for the PEDOT coating, and 40–60 nm could be the optimal coating thickness. In addition, our cycling test results agree with recent studies (Figure 5c), which show that the capacity fading rate decreases with an increase in primary LiCoO<sub>2</sub> particle size.

The evolution of cell impedance and Li apparent diffusion coefficient during cycling was tested to further elucidate the effect of polymer coatings on the Li<sup>+</sup> kinetics in LiCoO<sub>2</sub> electrodes. After 60 cycles, the overall impedance of all the LiCoO<sub>2</sub> electrodes increases by more than 2 orders of magnitude (Figure 5d). The PEDOT coating largely inhibits the growth of the impedance, while the copolymer increases impedance, and the PDVB has little effect. Figure 5e shows the evolution of the apparent diffusion coefficient of Li (*D*<sub>Li</sub>) in different LiCoO<sub>2</sub> electrodes measured from the galvanostatic intermittent titration technique (GITT) (Figure S10).<sup>29</sup> The *D*<sub>Li</sub> in the pristine LiCoO<sub>2</sub> decreases by 2 orders of magnitude (from 10<sup>-11</sup> to 10<sup>-13</sup> cm<sup>2</sup> s<sup>-1</sup>) after 80 cycles. The PEDOT coating decelerates the decrease of *D*<sub>Li</sub>, while the PDVB coating has no significant effect, and the copolymer accelerates the degradation rate of *D*<sub>Li</sub>. The improved *D*<sub>Li</sub> retention by the PEDOT coating matches well with the amount of Co element dissolution measured through inductively coupled plasma mass spectrometry measurement (ICP-MS), which shows that the PEDOT coating reduces the Co dissolution from 0.27% to 0.08% in LiCoO<sub>2</sub> after 40 cycles. Slowing down this degradation process could explain why PEDOT coating increases LiCoO<sub>2</sub> cycle life, as elaborated further in the next section.

There is general disagreement on the degradation mechanisms of LiCoO<sub>2</sub> during high voltage cycling. For example, Chen and Dahn first demonstrated that the capacity

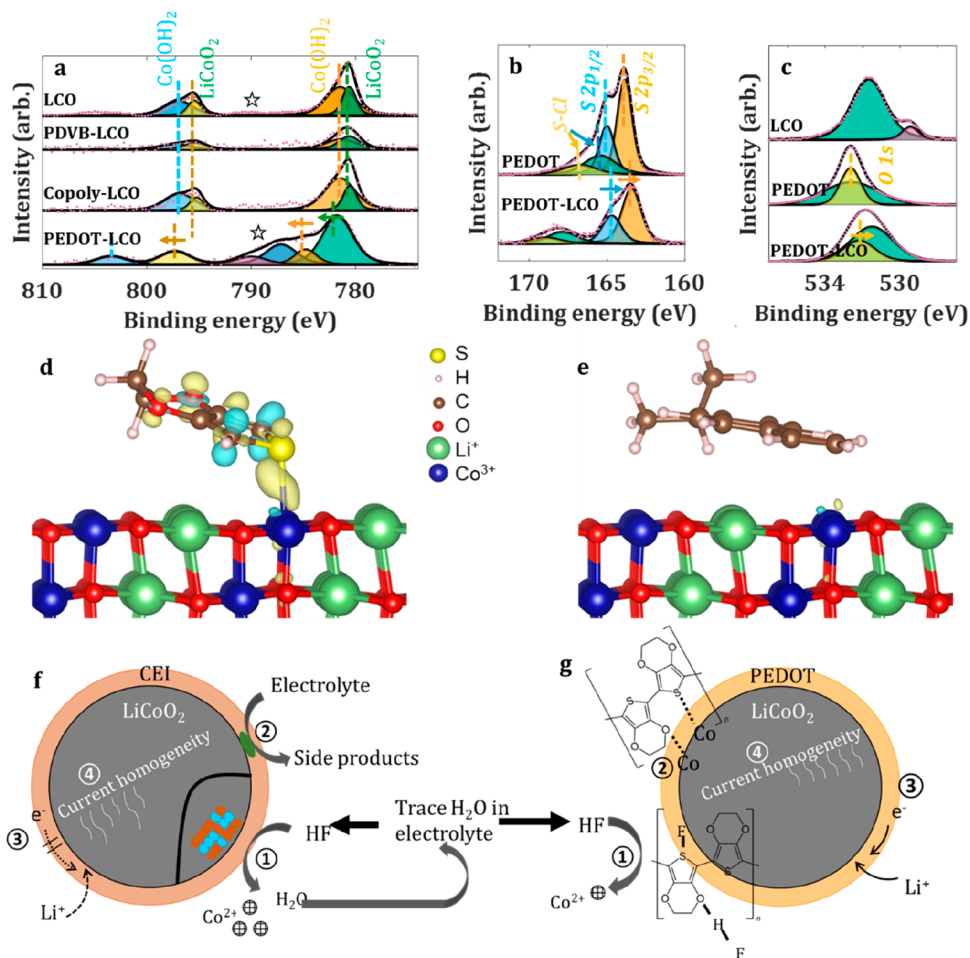


**Figure 6.** Experimental results and DFT calculations of the interactions between CVD polymers and LiCoO<sub>2</sub>. (a–c) XPS data for the Co 2p (a), S 2p (b), and O 1s (c) in different samples. Measurement data (dots) are fitted by several individual Lorentzian/Gaussian functions (colored regions). The combined spectra from these color shaded regions are shown as an envelope that matches well with experimental data (dots). (d, e) Electron density difference plots for EDOT (d) and DVB (e) binding to the LiCoO<sub>2</sub> surface calculated with DFT and displayed using an isovalue of 0.01. Yellow regions correspond to an electron density gain, and blue corresponds to an electron density loss. (f, g) Schematics to summarize the underlying mechanisms for improved LiCoO<sub>2</sub> cycling stability. The PEDOT coating reduces Co dissolution by sequestering HF in the electrolyte (①), inhibits electrolyte decomposition by forming chemical bonds with Co (②), slowing down kinetics degradation by providing fast transport channels for Li<sup>+</sup> and electrons (③), and alleviates mechanical degradation by increasing current homogeneity (④).

loss of LiCoO<sub>2</sub> (with an upper cutoff potential of 4.5 V) is mainly due to the interfacial impedance growth between LiCoO<sub>2</sub> and the surrounding electrolyte, resulting from side reactions between LiPF<sub>6</sub>-based electrolyte and LiCoO<sub>2</sub> surface impurities.<sup>30</sup> Amatucci et al. reported that the full extraction of Li ( $x = 0$ ) from Li<sub>x</sub>CoO<sub>2</sub> does not compromise its structure.<sup>26</sup> However, Liu et al. attributed the fast capacity fading of LiCoO<sub>2</sub> to its structural instability.<sup>31</sup> Our result suggests that selecting the right polymer artificial coating to modify the EEI is critical to the electrochemical performance of LiCoO<sub>2</sub>. The surface can mediate bulk structural changes (Figure 4) and, thus, is crucial to the electrochemical performance of LiCoO<sub>2</sub> for high-voltage cycling stability.

**Interactions between Polymer Coatings and LiCoO<sub>2</sub> Electrodes.** To understand the improved cycling stability from the PEDOT coating, we studied the interaction between polymer coatings and LiCoO<sub>2</sub>. Figure 6a–c compares XPS patterns of Co, S, and O in different samples. The binding energies of these XPS peaks are fitted via Lorentzian/Gaussian functions, and the fitted values are listed in Table S7. Pristine LiCoO<sub>2</sub> has Co<sup>3+</sup> 2p peaks at 780.61 and 795.45 eV. These

peaks are not affected by the PDVB and the copolymer coating, but the PEDOT coating increases the binding energies to 781.72 and 797.31 eV. Figure 6b,c shows that the S 2p and O 1s binding energies for PEDOT on LiCoO<sub>2</sub> are smaller than those for a PEDOT film deposited on a silicon wafer, which interacts weakly with the polymer. These results suggest that the Co at the surface of LiCoO<sub>2</sub> forms chemical/covalent bonds with S and O present in PEDOT. These bonds can inhibit the dissolution of cobalt species from LiCoO<sub>2</sub> during its cycling and prevent electrolyte decomposition.<sup>32</sup>

DFT calculations were further applied to understand the electrode-polymer interactions in the LiCoO<sub>2</sub>–PEDOT and the LiCoO<sub>2</sub>–PDVB systems. The repeating unit of PEDOT/PDVB (monomer) was utilized to reduce the computational cost. Figure 6d,e shows the structure constructions that have the minimum global Gibbs free energies for the two systems. Interactions between EDOT and the LiCoO<sub>2</sub> surface impact the electronic state of the EDOT molecule and the closest Co atom on the LiCoO<sub>2</sub> surface, while only small changes in electronic structure are observed for DVB. The binding energy of the system can be obtained from eq 3. Table S8 decomposes

the binding energies of both molecules into their electronic and dispersion components. Only 4% of the DVB-LiCoO<sub>2</sub> binding energy is due to the electronic interactions (−0.05 eV out of −1.29 eV), while 32% of the EDOT-LiCoO<sub>2</sub> binding energy is due to the electronic interactions (−0.44 eV out of −1.36 eV). The results suggest that the S in EDOT forms chemical bonds with Co on the surface of LiCoO<sub>2</sub>, while DVB interacts with LiCoO<sub>2</sub> almost entirely through van der Waals interactions.

$$\Delta E_{\text{bind}} = E_{\text{total}}(\text{surface} + \text{molecule}) - E_{\text{total}}(\text{surface}) - E_{\text{total}}(\text{molecule}) \quad (3)$$

where  $\Delta E_{\text{bind}}$  is the binding energy between LiCoO<sub>2</sub> and a monomer;  $E_{\text{total}}(\text{surface} + \text{molecule})$  is the total electronic energy of the optimized surface and adsorbate,  $E_{\text{total}}(\text{surface})$  and  $E_{\text{total}}(\text{molecule})$  are the total energy of the optimized surface and molecule when separated.

Figure 6f,g summarizes the mechanisms of the improved LiCoO<sub>2</sub> cycling stability by the PEDOT artificial coating. First, the dioxane ring on PEDOT can chemically coordinate HF in the electrolyte, which significantly decreases the concentration of HF and reduces the dissolution of Co from LiCoO<sub>2</sub>.<sup>7</sup> In comparison, the pristine LiCoO<sub>2</sub> goes through an HF generation-corrosion loop, resulting in continuous transition metal dissolution during cycling tests. We measured the percentage of Co dissolution from LiCoO<sub>2</sub> using ICP–MS measurement. The result shows that the 10 nm thick PEDOT coating reduced the Co dissolution from 0.27% to 0.08% after 40 cycles. The observed reduced Co dissolution agrees well with the existing study that shows surface engineering can reduce Co dissolution from LiCoO<sub>2</sub> during a high voltage cycling test.<sup>33</sup> Second, the PEDOT forms chemical bonds with Co present in LiCoO<sub>2</sub>. It has been reported that transition metals in battery cathodes are the active sites for electrolyte decomposition.<sup>32</sup> Hence, these chemical bonds can alleviate parasitic reactions between electrolyte and LiCoO<sub>2</sub>. Third, as PEDOT is a good conductor for electrons and Li<sup>+</sup>, it provides channels for the necessary transport of electrons and Li<sup>+</sup> in LIBs. These channels could therefore reduce the kinetics degradation of the LiCoO<sub>2</sub> during cycling. Finally, the PEDOT coating improves the homogeneity of current distribution over the LiCoO<sub>2</sub> electrode and reduces the local current density for active regions in LiCoO<sub>2</sub>. In comparison, the high flux of Li insertion/extraction from pristine LiCoO<sub>2</sub> would generate fast and nonuniform mechanical stress/strain oscillation during cycling. Such mechanical stress could lead to microcracks in LiCoO<sub>2</sub> particles and eventually mechanical fatigue of the LiCoO<sub>2</sub> electrode.<sup>34</sup>

**Design Rules for Engineering Polymer Artificial Coatings.** The three CVD polymer coatings we examined demonstrate different effects on the electrochemical performance of the LiCoO<sub>2</sub> electrode. The PEDOT artificial coating improves rate capability and cycling stability, the PDVB coating has no significant effect, and the P(PFDA-co-DVB) coating aggravates both performance metrics. By investigating the compositions and properties of these CVD polymers, uncovering the interactions between polymer coatings and Li<sup>+</sup>, and understanding the interactions between polymer coatings and LiCoO<sub>2</sub>, we can provide the following rules for selecting/designing polymers as artificial coatings for battery cathodes:

- (1) A polymer should provide fast transport channels for Li<sup>+</sup> and electrons to promote their transport in LIBs. This requires the functional groups in a polymer to have

reasonable binding energy with Li<sup>+</sup> and sufficient binding sites for Li<sup>+</sup>. For instance, the binding energy of Li<sup>+</sup> in PEDOT (−2.17 eV) is much lower than those in PDVB and P(PFDA-co-DVB), which helps the transport of Li<sup>+</sup> in the PEDOT polymer matrix. Additionally, PEDOT has almost twice the number of binding sites for Li<sup>+</sup> compared to P(PFDA-co-DVB). This reduces the hopping distance of Li<sup>+</sup> from one site to its neighbors and, thus, improves the transport of Li<sup>+</sup> in the polymer matrix. The polymer should be conjugated, i.e., conducting or at least semiconducting, to promote the transport of electrons in cathodes.

- (2) A polymer must form chemical bonds with the transition metals on the surface of the cathodes. Transition metals have been reported as the active sites for electrolyte decomposition.<sup>32</sup> The chemical bonds between transition metals and polymers can alleviate parasitic reactions between electrolyte and cathodes. This requires the polymer to have functional groups that serve as sigma donors or both  $\sigma$  and  $\pi$  donors. For instance, PEDOT has dioxane and thioether functional groups that chemically bond with Co on the surface of LiCoO<sub>2</sub>, as indicated by XPS measurement and DFT calculations. In comparison, PDVB interacts with LiCoO<sub>2</sub> through only van der Waals force.
- (3) A polymer must have functional groups that sequester HF. HF is a common side product in LiPF<sub>6</sub>-based electrolytes that reacts with battery cathodes. This reaction leads to transition metals dissolution and generates side products, like LiF, that block Li<sup>+</sup> transport and increase the impedance. The dioxane ring in PEDOT serves as an HF coordination site by forming O–H–F covalent bonds. For example, with such interactions, the Co dissolution is reduced from 0.27% to 0.08% after 40 cycles by a 10 nm thick PEDOT artificial coating.
- (4) A polymer must be electrochemically stable at high voltages (>4.5 V) to be compatible with emerging state-of-art cathode materials. The electrochemical stability window is a fundamental consideration for choosing polymers as artificial coatings and solid electrolytes in batteries.<sup>35</sup> PEDOT is stable with 4.6 V high voltage cathodes.<sup>7</sup> In comparison, the poor cycling stability of the P(PFDA-co-DVB)-coated LiCoO<sub>2</sub> might be from the poor electrochemical stability of the copolymer at high voltage.

## CONCLUSIONS

We studied Li<sup>+</sup> kinetics in artificial coatings and at EEIs using a comprehensive array of experimental techniques assisted by DFT calculations. By providing fast transport channels for Li<sup>+</sup> and electrons, we show that carefully selected coatings (in this case, CVD-grown PEDOT) can improve current homogeneity in the LiCoO<sub>2</sub> electrode during cycling and significantly increases its rate capability. Here, our techniques improve the 4.5 V cycle life by over 1700%. The development of next-generation electric vehicles is limited by cathodes with fast charging ability and long cycling life. Our findings provide a practical approach to overcome these limitations by promoting the Li<sup>+</sup> transport at EEIs and stabilizing the EEIs during cycling using polymer coatings. Although only three polymers have been explored in this study, the design rules derived from our

mechanistic studies will guide the selection of ideal polymer materials for advanced cathodes with fast charging ability and long cycle life. Because of their mild synthesis conditions and ability to form conformal coatings with precisely controlled thickness and chemical composition, CVD polymers can further improve the performance of battery anodes, solid electrolytes, and complex interfaces inside critical renewable energy systems solar cells and fuel cells.

## EXPERIMENTAL SECTION

**Chemical Vapor Deposition (CVD) Polymerization.** The iCVD system (GVD Corp.) was utilized to synthesize PDVB and P(PFDA-co-DVB), while the oCVD system (GVD Corp.) was applied to synthesize PEDOT. The schematics of the two systems are shown in Figure 1, and the details of synthesizing PDVB and PEDOT could be found in Table S1 and our previous publication.<sup>2</sup> All chemicals were purchased from Sigma-Aldrich without further purification, including DVB, EDOT, PFDA, *t*-butylperoxide (TBPO), and FeCl<sub>3</sub>. To synthesize PEDOT, the flow rate of EDOT monomer and Ar carrier gas was 1 and 2 sccm. The chamber pressure was held constant at 50 mTorr, the stage temperature was controlled to 130 °C, and the temperature of the crucible was 200 °C that contained FeCl<sub>3</sub> oxidant. The thickness of the film was controlled by varying deposition time. To grow PDVB, the flow rate of DVB monomer, TBPO initiator, and Ar carrier gas were 1.3, 2.0, and 8.5 sccm, respectively. The chamber pressure was held constant at 500 mTorr, the stage temperature was controlled to 25 °C, and the filament temperature was 230 °C to cleave the TBPO initiator. Such a condition gives the ratio of 0.15 between monomer partial pressure ( $P_m$ ) to saturation pressure ( $P_{sat}$ ) that is low enough to ensure conformal coating for complex structure. As for P(PFDA-co-DVB) synthesis, the flow rates of PFDA monomer, DVB monomer, TBPO initiator, and Ar carrier gas were 0.16, 0.6, 1.0, and 0.4 sccm, respectively. The chamber pressure was held constant at 100 mTorr, the stage temperature was controlled to 30 °C, and the filament temperature was 230 °C to cleave the TBPO initiator. The  $P_m/P_{sat} = 0.06$  for DVB and  $P_m/P_{sat} = 0.10$  for PFDA monomer that ensured a conformal coating for LiCoO<sub>2</sub> electrodes. The thicknesses of iCVD films were monitored in real-time using in situ laser interferometry on a silicon monitor wafer. The deposition was terminated by turning off the filament after achieving the desired thickness.

**Material Characterization.** SEM and EDS were conducted on Quanta 600 (Thermo Fisher Scientific) using 5.0–10.0 kV accelerating voltages, depending on the conductivity of our materials. The spot size was around 10 nm. The trench that we used to study the conformal coating was 6 μm deep and 1 μm wide with an 8 μm spacing between the trenches. A 2 nm thick platinum was coated on the surface of the samples to reduce the surface charging during SEM imaging. TEM was carried out on a JEOL 2000EX electron microscope operating at 200 kV in a bright field. Copper grids (300 mesh, TED PELLA, Inc.) coated with an ~50 Å thick amorphous carbon film were utilized to hold LiCoO<sub>2</sub> particles. The whole grids were placed in CVD chambers to be coated with polymers. Then, TEM images were taken on these samples. The thicknesses of transparent PDVB and P(PFDA-co-DVB) on silicon wafer were measured by ellipsometry, while the thickness of optical non-transparent PEDOT on a silicon wafer was measured by profilometry. In addition, the polymer coating thickness on LiCoO<sub>2</sub> particles was measured by TEM because of their rough surface. As for the different substrates, the polymer film is about two times thicker on a silicon wafer than that on LiCoO<sub>2</sub> particles under the same experimental conditions. XPS measurements were tested using monochromatized Al K  $\alpha$  radiation (1486.7 eV) as the X-ray source. The base pressure was 10<sup>-8</sup> Pa, and the spot diameter was 600 μm during the test. Three survey scans with a step size of 1.0 eV were collected, followed by 10 high-resolution scans with a step size of 0.1 eV for target elements. All the binding energies were calibrated by the C 1s hydrocarbon peak (284.8 eV). The obtained XPS data were analyzed by Avantage

software with the following parameters: full width at half-maximum (eV) = 0.5:3.5 and Lorentzian/Gaussian = 30%.

**Electrochemical Characterization.** The electrochemical performance was measured in CR2016 coin cells. All the raw materials were purchased from MTI Corporation unless specified. 80% LiCoO<sub>2</sub>, 10% polyvinylidene fluoride binder, and 10% super-P conductive agent were mixed in *N*-methyl-2-pyrrolidone (NMP). The slurry was then cast onto Al current collectors. The typical load of the active material was 3–4 mg cm<sup>-2</sup>. After drying in a 110 °C vacuum oven for 12 h, disks with a diameter of 14 mm were punched and used as cathodes. Coin cells were assembled in a glovebox (Thermo Fisher Scientific) with H<sub>2</sub>O and O<sub>2</sub> level less than 0.5 ppm using a lithium chip as the anode, Cellgard separator, and around 100 μL of 1 M LiPF<sub>6</sub> dissolved in ethylene carbonate/diethyl carbonate (1:1 in volume) as the electrolyte. The PDVB-coated and copolymer-coated LiCoO<sub>2</sub> electrodes were utilized directly, while the PEDOT-coated LiCoO<sub>2</sub> was rinsed in methanol for 5 min to remove residual monomer and oxidant. The electrochemical performances of coin cells were tested using a VMP3 (Biologic Company) and LAND battery cyclers (LAND Electronics Co., Ltd.). All cells were cycled using a C/10 rate three times within the 3.0–4.2 V voltage range before conducting other tests. All tests were conducted at 20 °C unless otherwise stated. The rate capability was measured using the constant-current (CC) constant-voltage (CV) charging protocol followed by CC protocol at different C-rates within 3.0–4.2 V. The current during CC charging is C/3, and the cutoff current during CV charging is C/100. EIS measurement was conducted at 4.0 V (open circuit voltage) for all cells by applying an ac voltage of 10 mV amplitude over the frequency range of 100 kHz to 10 mHz. A high voltage cycling test was carried out within the voltage range of 3.0 to 4.5 V at C/2 using a CC protocol for both charging and discharging. The GITT measurement was conducted by applying a 10 min galvanostatic charge/discharge pulse (C/10) followed by a 2 h relaxation within the voltage range of 3.0 to 4.5 V.

Aged (after 40 cycles) coin cells were disassembled in an argon-filled glovebox with O<sub>2</sub> and H<sub>2</sub>O level below 0.5 ppm to measure the Co dissolution from LiCoO<sub>2</sub> electrodes after cycling. All components were immersed in 10 mL dimethyl carbonate (DMC) for 3 days. Two mL of the solution was diluted in 6 mL HNO<sub>3</sub> (65%). The mixed solution was heated to 120 °C in a vacuum chamber until all the liquid disappeared. The remaining white/yellow powder was collected and dissolved in 10 mL deionized water, followed by 30 min of ultrasonic treatment. Finally, 6 mL solution was filtered through a 0.45 μm filter, and 0.2 mL HNO<sub>3</sub> (70%) was added to the solution before conducting the inductively coupled plasma mass spectrometry (ICP-MS, Agilent Technologies 7700 Series).

**Neutron Reflectometry.** Neutron reflectometry (NR) experiments were performed on the MAGIK reflectometer at the National Institute of Standards and Technology (NIST) Center for Neutron Research (NCNR).<sup>36</sup> Specular NR measures the reflected intensity of a collimated, monochromatic neutron beam scattered from the sample surface. Fitting the variations in reflected intensity as a function of scattering vector yields a one-dimensional depth profile of the sample scattering length density (SLD), which is a function of the sample composition. Samples were analyzed in a helium-filled aluminum chamber, and NR data was collected on the unlithiated polymers.

NR data was fit using Refl1d.<sup>37</sup> In this program, a model SLD profile is proposed as a layered structure of material “slabs”. Each slab is described by three parameters: (i) real and imaginary SLD (which are related by composition), (ii) thickness (in Å), and (iii) width of the interface with the next layer (i.e., the interfacial roughness and interdiffusion, in Å). In this study, the interface width is fit as a fraction of the thinnest layer to which it is in contact. Fitting of the models is completed using the DREAM, a differential evolution algorithm.<sup>37</sup> DREAM randomly generates many models within a given parameter space and allows this population to “evolve” over a user-defined number of generations. The calculated resultant population density represents the probability density because the probability of retaining a given parameter set is proportional to its

likelihood. This method serves as a robust approach to sample multidimensional parameter spaces without selecting only a nearby local minimum (as can occur in gradient descent approaches), is able to identify multiple best fits when more than one solution is statistically feasible, and provides accurate uncertainty estimates for fitted parameters, as it explicitly preserves interparameter correlations. Samples were fit independently of one another, with zero, one, two, three, and, in special cases, four-slab models. In most cases, the parameters of these slabs were allowed to vary over a wide range to account for possible compositional variations and thicknesses of the polymer films. Models with and without the native oxide,  $\text{SiO}_x$ , were tested. In the  $\text{SiO}_x$  models, the SLD parameter for this layer was limited to a range of 2.0 to 3.0. The quality of a model's fit is determined by comparing it to the measured profile and calculating the  $\chi^2$ , and the difference between fits is evaluated using Bayesian Information Criteria.<sup>38–40</sup>

**Neutron Depth Profiling.** NDP data was acquired at Neutron Guide 5 (NG5), Cold Neutron Depth Profiling station at the NCNR in NIST.<sup>41</sup> Samples were mounted behind a 6.0 mm circular, Teflon aperture. Each sample was irradiated at a near-constant fluence rate of cold neutrons ( $\sim 10^9 \text{ cm}^{-2} \text{ s}^{-1}$ ), and all experiments were conducted under vacuum and 20 °C. NDP spectra were collected for  $\sim 4$  h per spot.  $^6\text{Li}$  nuclear reaction triton (t) and alpha ( $\alpha$ ) particles were detected using a circular transmission-type silicon surface-barrier detector that was positioned  $\sim 120$  mm from the sample surface. Each spectrum was corrected for dead time ( $\sim 0.01\%$ ) and background signals.

Interactions of the triton ( $^3\text{H}$ ) particles with the polymers were modeled in SRIM utilizing the densities obtained by NR (see Figure S3).<sup>42</sup> Processed profiles were used to estimate the relative penetration of Li into the polymers. Li concentrations were calculated in reference to the known concentration of  $^{10}\text{B}$  in a B-implanted concentration standard. Final reported uncertainties are reported to 2 $\sigma$  and were calculated from experimental counting statistics.

**Density Functional Theory (DFT) Calculation.** DFT calculations on polymer cluster models were performed using Gaussian 16.<sup>43</sup> Structures were optimized at the B3LYP/6-31G\* level with D3 dispersion<sup>44</sup> and Becke-Johnson damping (D3BJ).<sup>45</sup> The energy of every fully optimized structure was recalculated at the B3LYP/cc-pVDZ level with D3BJ dispersion.<sup>46</sup> The vibrational frequencies of optimized molecular structures were calculated at the B3LYP/6-31+G\* level with D3BJ dispersion and were used to confirm that all molecular structures were fully optimized. The frequencies were then used within the ideal gas, rigid rotor, and harmonic oscillator approximations to calculate free energy contributions for each structure.<sup>47</sup> The binding sites presented in this work were identified by systematically placing  $\text{Li}^+$  at different binding sites and fully optimizing each structure to identify the most favorable binding site and orientation.

All periodic DFT calculations that contained  $\text{LiCoO}_2$  surfaces were performed using the Vienna ab initio simulation package (VASP).<sup>48–50</sup> These calculations utilized the Perdew–Burke–Ernzerhof (PBE),<sup>51,52</sup> GGA exchange–correlation functional, and the projector augmented wave (PAW) method.<sup>53</sup> D2 dispersion was utilized to account for Vander Waals interactions.<sup>54</sup> We used the on-site Hubbard U model ( $U-J = 3.3 \text{ eV}$ ) to account for the overdelocalization of electron density present in DFT.<sup>55</sup>

We modeled the adsorption of EDOT and DVB to a 4-layer thick (1014)  $\text{LiCoO}_2$  surface composed of 48  $\text{LiCoO}_2$  formula units in a unit cell with  $a = 18.0 \text{ \AA}$ ,  $b = 11.26 \text{ \AA}$ ,  $\gamma = 108.22^\circ$ , and 20  $\text{ \AA}$  of vacuum space. The (1014)  $\text{LiCoO}_2$  surface was selected because it has been shown to be stable at a variety of experimental conditions<sup>56</sup> and allows for  $\text{Li}^+$  to be transported away from the surface.<sup>32</sup> Using a  $\gamma$ -point and an energy cutoff of 800 eV gave well-converged energies for the  $\text{LiCoO}_2$  surface with and without adsorbates present. All structures were fully optimized using the default VASP convergence criteria. The bottom 2 layers of the  $\text{LiCoO}_2$  slab were fixed to bulk  $\text{LiCoO}_2$  coordinates. We compared the energies for a variety of different EDOT and DVB orientations at different adsorption sites on the surface to locate low energy adsorbate structures. Electron density

difference plots were calculated by subtracting the electron density of the surface and EDOT or DVB from the electron density of the full system. The surface area of the EDOT and DVB molecules that interacted with the  $\text{LiCoO}_2$  surface was estimated by placing spheres ( $R =$  Vander Waals radii,  $R_{\text{H}} = 1.20 \text{ \AA}$ ,  $R_{\text{O}} = 1.52 \text{ \AA}$ ,  $R_{\text{C}} = 1.70 \text{ \AA}$ ,  $R_{\text{S}} = 1.80 \text{ \AA}$ ) on each atom of the fully optimized EDOT/DVB molecule adsorbed to the  $\text{LiCoO}_2$  surface. These spheres were projected onto the XY plane (the plane that is parallel to the surface) to obtain the approximate surface area of each molecule interacting with the surface.

**Operando ED-XRD Measurement.** Operando energy dispersive X-ray diffraction (ED-XRD) measurements were conducted using beamline 6-BM-A at the Advanced Photon Sources in Argonne National Laboratory. The white X-ray radiation was generated by bending magnets with an energy range of 20–200 keV. The detection angles were  $2.99^\circ$  and  $6.70^\circ$  for two Canberra germanium detectors to collect the diffraction pattern. The operando experiment is conducted using a transmission geometry and provides spatial and temporal mapping capabilities. Coin cells were cycled at C/2 within 3.0 to 4.5 V, during which ED-XRD pattern was collected for 60 s at one point. The height (10  $\mu\text{m}$ ) and width (2 mm) of the incident X-ray beam were kept constant during the measurement. Three points at different amplitudes, corresponding to different locations to the separator, were measured continuously, followed by a 60 s rest. The XRD data were collected until the cells went through one full cycle.

## ■ ASSOCIATED CONTENT

### Supporting Information

The Supporting Information is available free of charge at <https://pubs.acs.org/doi/10.1021/acsami.0c20978>.

$\text{LiCoO}_2$  powder information, XPS of synthesized polymers, NR results, NDP results, cycling curves at different C-rates, EIS data at different temperature, and the fitted results, DFT calculation for polymers and ions in the electrolyte, operando ED-XRD at different locations, cycling data at different conditions, GITT measurement, CVD polymerization synthesis conditions, NR fitting results, NR measurement for different polymer thin films, EIS fitted results, the number of  $\text{Li}^+$  binding sites in polymers, cycling stability of  $\text{LiCoO}_2$  electrodes in existing literature, XPS binding energy for elements in different samples, and DFT calculation for the interaction between monomers and  $\text{LiCoO}_2$  (PDF) Table S2, neutron reflectometry fitting for the three CVD polymer thin films (XLSX)

## ■ AUTHOR INFORMATION

### Corresponding Author

B. Reeja-Jayan – Department of Mechanical Engineering, Carnegie Mellon University, Pittsburgh, Pennsylvania 15213, United States; [orcid.org/0000-0002-6959-6290](https://orcid.org/0000-0002-6959-6290); Email: [bjayan@andrew.cmu.edu](mailto:bjayan@andrew.cmu.edu)

### Authors

Laisuo Su – Department of Mechanical Engineering, Carnegie Mellon University, Pittsburgh, Pennsylvania 15213, United States; [orcid.org/0000-0002-9307-9357](https://orcid.org/0000-0002-9307-9357)

Jamie L. Weaver – National Institute of Standards and Technology, Material Measurement Laboratory, Gaithersburg, Maryland 20899, United States; [orcid.org/0000-0002-6762-0568](https://orcid.org/0000-0002-6762-0568)

Mitchell Groenenboom – National Institute of Standards and Technology, Material Measurement Laboratory, Gaithersburg, Maryland 20899, United States; [orcid.org/0000-0002-7859-107X](https://orcid.org/0000-0002-7859-107X)

**Nathan Nakamura** – Department of Mechanical Engineering, Carnegie Mellon University, Pittsburgh, Pennsylvania 15213, United States

**Eric Rus** – National Institute of Standards and Technology, Center for Neutron Research, Gaithersburg, Maryland 20899, United States; [orcid.org/0000-0001-5031-6888](https://orcid.org/0000-0001-5031-6888)

**Priyanka Anand** – Department of Materials Science & Engineering, Carnegie Mellon University, Pittsburgh, Pennsylvania 15213, United States

**Shikhar Krishn Jha** – Department of Mechanical Engineering, Carnegie Mellon University, Pittsburgh, Pennsylvania 15213, United States

**John S. Okasinski** – Advanced Photon Source, Argonne National Laboratory, Lemont, Illinois 60439, United States

**Joseph A. Dura** – National Institute of Standards and Technology, Center for Neutron Research, Gaithersburg, Maryland 20899, United States; [orcid.org/0000-0001-6877-959X](https://orcid.org/0000-0001-6877-959X)

Complete contact information is available at:  
<https://pubs.acs.org/10.1021/acsami.0c20978>

## Notes

The authors declare no competing financial interest.

## ACKNOWLEDGMENTS

This work was supported by the National Science Foundation (NSF) CAREER Award (CMMI1751605) and INCUBATE seed funding from Carnegie Mellon University. B.R.-J. acknowledges the Wilton E. Scott Institute for Energy Innovation for Faculty Fellowship. The authors acknowledge the use of the Materials Characterization Facility at Carnegie Mellon University (CMU) supported by grant MCF-677785. N.N. is supported by a National Defense Science and Engineering Graduate (NDSEG) Fellowship. This research used 6-BM-A beamline and other resources in Advanced Photon Source, Argonne National Laboratory under Contract No. DE-AC02-06CH11357. The authors thank Prof. Jay F Whitacre and Prof. Shawn Litster at CMU for sharing some of their equipment and lab facilities, Dr. Jiang Xu for his assistance with ICP-MS data collection, and Dr. Joel Gillespie from the University of Pittsburgh Materials Characterization Laboratory for the access to the XPS spectrometer. The authors acknowledge Prof. Venkat Viswanathan in CMU for constructive discussion and guidance on experimental results and DFT calculations. Certain commercial products are identified in this work to specify the experimental procedures in adequate detail. This identification does not imply recommendation or endorsement by the authors or by the National Institute of Standards and Technology (NIST), nor does it imply that the products identified are necessarily the best available for the purpose. Contributions of the NIST are not subject to copyright.

## REFERENCES

- (1) Gauthier, M.; Carney, T. J.; Grimaud, A.; Giordano, L.; Pour, N.; Chang, H.; Fenning, D. P.; Lux, S. F.; Paschos, O.; Bauer, C.; Maglia, F.; Lupart, S.; Lamp, P.; Shao-Horn, Y. Electrode-Electrolyte Interface in Li-Ion Batteries: Current Understanding and New Insights. *J. Phys. Chem. Lett.* **2015**, *6*, 4653–4672.
- (2) Su, L.; Smith, P. M.; Anand, P.; Reeja-Jayan, B. Surface Engineering of a LiMn<sub>2</sub>O<sub>4</sub> Electrode Using Nanoscale Polymer Thin Films Via Chemical Vapor Deposition Polymerization. *ACS Appl. Mater. Interfaces* **2018**, *10*, 27063–27073.

- (3) Li, Y.; Chen, H.; Lim, K.; Deng, H. D.; Lim, J.; Fraggadakis, D.; Attia, P. M.; Lee, S. C.; Jin, N.; Moškon, J.; Guan, Z.; Gent, W. E.; Hong, J.; Yu, Y.; Gaberšček, M.; Islam, M. S.; Bazant, M. Z.; Chueh, W. C. Fluid-Enhanced Surface Diffusion Controls Intraparticle Phase Transformations. *Nat. Mater.* **2018**, *17*, 915–922.

- (4) Shen, B. H.; Wang, S.; Tenhaeff, W. E. Ultrathin Conformal Polycyclosiloxane Films to Improve Silicon Cycling Stability. *Sci. Adv.* **2019**, *5* (7), No. w4856.

- (5) Su, L.; Jha, S. K.; Phuah, X. L.; Xu, J.; Nakamura, N.; Wang, H.; Okasinski, J. S.; Reeja-Jayan, B. Engineering Lithium-Ion Battery Cathodes for High-Voltage Applications Using Electromagnetic Excitation. *J. Mater. Sci.* **2020**, *55*, 12177–12190.

- (6) Wang, L.; Chen, B.; Ma, J.; Cui, G.; Chen, L. Reviving Lithium Cobalt Oxide-Based Lithium Secondary Batteries-Toward a Higher Energy Density. *Chem. Soc. Rev.* **2018**, *47*, 6505–6602.

- (7) Xu, G.; Liu, Q.; Lau, K. K. S.; Liu, Y.; Liu, X.; Gao, H.; Zhou, X.; Zhuang, M.; Ren, Y.; Li, J.; Shao, M.; Ouyang, M.; Pan, F.; Chen, Z.; Amine, K.; Chen, G. Building Ultraconformal Protective Layers on Both Secondary and Primary Particles of Layered Lithium Transition Metal Oxide Cathodes. *Nat. Energy.* **2019**, *4* (6), 484–494.

- (8) Kalluri, S.; Yoon, M.; Jo, M.; Park, S.; Myeong, S.; Kim, J.; Dou, S. X.; Guo, Z.; Cho, J. Surface Engineering Strategies of Layered LiCoO<sub>2</sub> Cathode Material to Realize High-Energy and High-Voltage Li-Ion Cells. *Adv. Energy Mater.* **2017**, *7*, 1601507.

- (9) Wang, X.; Yushin, G. Chemical Vapor Deposition and Atomic Layer Deposition for Advanced Lithium Ion Batteries and Supercapacitors. *Energy Environ. Sci.* **2015**, *8*, 1889–1904.

- (10) Gleason, K. K. *CVD Polymers: Fabrication of Organic Surfaces and Devices*; John Wiley & Sons: New York, 2015.

- (11) Gleason, K. K. Organic Surface Functionalization by Initiated CVD (iCVD). Surface Modification of Polymers: Methods and Applications. In *Surface Modification of Polymers: Methods and Applications*; Wiley: New York, 2019, pp 107–134.

- (12) Gleason, K. K.; Wang, X. *Oxidative Chemical Vapor Deposition for Conjugated Polymers: Theory and Applications*; CRC Press: Boca Raton, FL, 2019, pp 587–611.

- (13) Lasia, A. *Electrochemical Impedance Spectroscopy and its Applications*; Springer: New York, 2014.

- (14) Tataru, R.; Karayaylali, P.; Yu, Y.; Zhang, Y.; Giordano, L.; Maglia, F.; Jung, R.; Schmidt, J. P.; Lund, L.; Shao-Horn, Y. The Effect of Electrode-Electrolyte Interface on the Electrochemical Impedance Spectra for Positive Electrode in Li-Ion Battery. *J. Electrochem. Soc.* **2019**, *166*, A5090–A5098.

- (15) Im, S. G.; Gleason, K. K. Systematic Control of the Electrical Conductivity of Poly(3,4-Ethylenedioxythiophene) Via Oxidative Chemical Vapor Deposition. *Macromolecules* **2007**, *40*, 6552–6556.

- (16) Smith, P. M.; Su, L.; Gong, W.; Nakamura, N.; Reeja-Jayan, B.; Shen, S. Thermal Conductivity of Poly(3,4-Ethylenedioxythiophene) Films Engineered by Oxidative Chemical Vapor Deposition (oCVD). *RSC Adv.* **2018**, *8*, 19348–19352.

- (17) Paxson, A. T.; Yagüe, J. L.; Gleason, K. K.; Varanasi, K. K. Stable Dropwise Condensation for Enhancing Heat Transfer Via the Initiated Chemical Vapor Deposition (iCVD) of Grafted Polymer Films. *Adv. Mater.* **2014**, *26*, 418–423.

- (18) Lepró, X.; Ehrmann, P.; Menapace, J.; Lotscher, J.; Shin, S.; Meissner, R.; Baxamusa, S. Ultralow Stress, Thermally Stable Cross-Linked Polymer Films of Polydivinylbenzene (PDVB). *Langmuir* **2017**, *33*, 5204–5212.

- (19) Lenz, A.; Kariis, H.; Pohl, A.; Persson, P.; Ojamäe, L. The Electronic Structure and Reflectivity of PEDOT:PSS From Density Functional Theory. *Chem. Phys.* **2011**, *384*, 44–51.

- (20) Zhang, J.; Su, L.; Li, X.; Ge, H.; Zhang, Y.; Li, Z. Lithium Plating Identification From Degradation Behaviors of Lithium-Ion Cells. *J. Electrochem.* **2016**, *22*, 607.

- (21) Zhuang, Q.; Xu, J.; Fan, X.; Dong, Q.; Jiang, Y.; Huang, L.; Sun, S. An Electrochemical Impedance Spectroscopic Study of the Electronic and Ionic Transport Properties of LiCoO<sub>2</sub> Cathode. *Chin. Sci. Bull.* **2007**, *52*, 1187–1195.

- (22) Nobili, F.; Dsoke, S.; Croce, F.; Marassi, R. An AC Impedance Spectroscopic Study of Mg-Doped LiCoO<sub>2</sub> at Different Temperatures: Electronic and Ionic Transport Properties. *Electrochim. Acta* **2005**, *50*, 2307–2313.
- (23) Suresh, P.; Shukla, A. K.; Munichandraiah, N. Temperature Dependence Studies of AC Impedance of Lithium-Ion Cells. *J. Appl. Electrochem.* **2002**, *32*, 267–273.
- (24) Angell, C. A. Mobile Ions in Amorphous Solids. *Annu. Rev. Phys. Chem.* **1992**, *43*, 693–717.
- (25) Moni, P.; Lau, J.; Mohr, A. C.; Lin, T. C.; Tolbert, S. H.; Dunn, B.; Gleason, K. K. Growth Temperature and Electrochemical Performance in Vapor-Deposited Poly(3, 4-Ethylenedioxythiophene) Thin Films for High-Rate Electrochemical Energy Storage. *ACS Applied Energy Materials.* **2018**, *1*, 7093–7105.
- (26) Amatuucci, G. G.; Tarascon, J. M.; Klein, L. C. CoO<sub>2</sub>, the End Member of the Li<sub>x</sub>CoO<sub>2</sub> Solid Solution. *J. Electrochem. Soc.* **1996**, *143*, 1114–1123.
- (27) Liu, L.; Chen, L.; Huang, X.; Yang, X.; Yoon, W.; Lee, H. S.; McBreen, J. Electrochemical and in Situ Synchrotron Xrd Studies on Al<sub>2</sub>O<sub>3</sub>-Coated LiCoO<sub>2</sub> Cathode Material. *J. Electrochem. Soc.* **2004**, *151*, A1344–A1351.
- (28) Xu, Y.; Hu, E.; Zhang, K.; Wang, X.; Borzenets, V.; Sun, Z.; Pianetta, P.; Yu, X.; Liu, Y.; Yang, X.; Li, H. In Situ Visualization of State-of-Charge Heterogeneity within a LiCoO<sub>2</sub> Particle that Evolves upon Cycling at Different Rates. *ACS Energy Lett.* **2017**, *2*, 1240–1245.
- (29) Weppner, W.; Huggins, R. A. Determination of the Kinetic Parameters of Mixed-Conducting Electrodes and Application to the System Li<sub>3</sub>Sb. *J. Electrochem. Soc.* **1977**, *124*, 1569–1578.
- (30) Chen, Z.; Dahn, J. R. Improving the Capacity Retention of LiCoO<sub>2</sub> Cycled to 4.5 V by Heat-Treatment. *Electrochem. Solid-State Lett.* **2004**, *7*, A11.
- (31) Liu, Q.; Su, X.; Lei, D.; Qin, Y.; Wen, J.; Guo, F.; Wu, Y. A.; Rong, Y.; Kou, R.; Xiao, X.; Aguesse, F.; Bareño, J.; Ren, Y.; Lu, W.; Li, Y. Approaching the Capacity Limit of Lithium Cobalt Oxide in Lithium Ion Batteries Via Lanthanum and Aluminium Doping. *Nat. Energy.* **2018**, *3* (11), 936–943.
- (32) Xie, Y.; Gao, H.; Gim, J.; Ngo, A. T.; Ma, Z.; Chen, Z. Identifying Active Sites for Parasitic Reactions at the Cathode-Electrolyte Interface. *J. Phys. Chem. Lett.* **2019**, *10*, 589–594.
- (33) Qian, J.; Liu, L.; Yang, J.; Li, S.; Wang, X.; Zhuang, H. L.; Lu, Y. Electrochemical Surface Passivation of LiCoO<sub>2</sub> Particles at Ultrahigh Voltage and Its Applications in Lithium-Based Batteries. *Nat. Commun.* **2018**, *9* (1), 1–11.
- (34) Li, Y.; Cheng, X.; Zhang, Y.; Zhao, K. Recent Advance in Understanding the Electro-Chemo-Mechanical Behavior of Lithium-Ion Batteries by Electron Microscopy. *Materials Today Nano.* **2019**, *7*, 100040.
- (35) Chen, L.; Venkatram, S.; Kim, C.; Batra, R.; Chandrasekaran, A.; Ramprasad, R. Electrochemical Stability Window of Polymeric Electrolytes. *Chem. Mater.* **2019**, *31*, 4598–4604.
- (36) Dura, J. A.; Pierce, D. J.; Majkrzak, C. F.; Maliszewskij, N. C.; McGillivray, D. J.; Losche, M.; O'Donovan, K. V.; Mihailescu, M.; Perez-Salas, U.; Worcester, D. L.; White, S. H. And/R: Advanced Neutron Diffractometer/Reflectometer for Investigation of Thin Films and Multilayers for the Life Sciences. *Rev. Sci. Instrum.* **2006**, *77*, 74301.
- (37) Kienzle, P. A.; Maranville, B. B.; O'Donovan, K. V.; Ankner, J. F.; N. F. Berk, C. F. M. Reflectometry Software. <https://www.nsl.gov/ncnr/reflectometry-software>. 2017.
- (38) DeCaluwe, S. C.; Kienzle, P. A.; Bhargava, P.; Baker, A. M.; Dura, J. A. Phase Segregation of Sulfonate Groups in Nafion Interface Lamellae, Quantified Via Neutron Reflectometry Fitting Techniques for Multi-Layered Structures. *Soft Matter* **2014**, *10*, 5763–5776.
- (39) Bogdan, M.; Ghosh, J. K.; Doerge, R. W. Modifying the Schwarz Bayesian Information Criterion to Locate Multiple Interacting Quantitative Trait Loci. *Genetics* **2004**, *167*, 989–999.
- (40) Schwarz, G. Estimating the Dimension of a Model. *Annals of Statistics.* **1978**, *6*, 461–464.
- (41) Lamaze, G.; Downing, R.; Langland, J.; Hwang, S. The New Cold Neutron Depth Profiling Instrument at Nist. *J. Radioanal. Nucl. Chem.* **1992**, *160*, 315–325.
- (42) Ziegler, J. F.; Biersack, J. P.; Ziegler, M. D. Srim, a Version of the Trim Program. *The Stopping and Range of Ions in Matter*, 2008.
- (43) Frisch, M. J.; Trucks, G. W.; Schlegel, H. B.; Scuseria, G. E.; Robb, M. A.; Cheeseman, J. R.; Scalmani, G.; Barone, V.; Petersson, G. A.; Nakatsuji, H.; Li, X.; Caricato, M.; Marenich, A. V.; Bloino, J.; Janesko, B. G.; Gomperts, R.; Mennucci, B.; Hratchian, H. P.; Ortiz, J. V.; Izmaylov, A. F.; Sonnenberg, J. L.; Williams, Ding, F.; Lipparini, F.; Egidi, F.; Goings, J.; Peng, B.; Petrone, A.; Henderson, T.; Ranasinghe, D.; Zakrzewski, V. G.; Gao, J.; Rega, N.; Zheng, G.; Liang, W.; Hada, M.; Ehara, M.; Toyota, K.; Fukuda, R.; Hasegawa, J.; Ishida, M.; Nakajima, T.; Honda, Y.; Kitao, O.; Nakai, H.; Vreven, T.; Throssell, K.; Montgomery, J. A., Jr.; Peralta, J. E.; Ogliaro, F.; Bearpark, M. J.; Heyd, J. J.; Brothers, E. N.; Kudin, K. N.; Staroverov, V. N.; Keith, T. A.; Kobayashi, R.; Normand, J.; Raghavachari, K.; Rendell, A. P.; Burant, J. C.; Iyengar, S. S.; Tomasi, J.; Cossi, M.; Millam, J. M.; Klene, M.; Adamo, C.; Cammi, R.; Ochterski, J. W.; Martin, R. L.; Morokuma, K.; Farkas, O.; Foresman, J. B.; Fox, D. J. *Gaussian 16*; Gaussian, Inc.: Wallingford, CT, 2016.
- (44) Grimme, S.; Antony, J.; Ehrlich, S.; Krieg, H. A Consistent and Accurate Ab Initio Parametrization of Density Functional Dispersion Correction (DFT-D) for the 94 Elements H-Pu. *J. Chem. Phys.* **2010**, *132*, 154104.
- (45) Grimme, S.; Ehrlich, S.; Goerigk, L. Effect of the Damping Function in Dispersion Corrected Density Functional Theory. *J. Comput. Chem.* **2011**, *32*, 1456–1465.
- (46) Dunning, T. H. Gaussian Basis Sets for Use in Correlated Molecular Calculations. I. The Atoms Boron through Neon and Hydrogen. *J. Chem. Phys.* **1989**, *90*, 1007–1023.
- (47) Cramer, C. J. *Essentials of Computational Chemistry: Theories and Models*; John Wiley & Sons Ltd.: New York, 2002, p 542.
- (48) Kresse, G.; Furthmüller, J. Efficient Iterative Schemes for Ab Initio Total-Energy Calculations Using a Plane-Wave Basis Set. *Phys. Rev. B: Condens. Matter Mater. Phys.* **1996**, *54*, 11169.
- (49) Kresse, G.; Furthmüller, J. Efficiency of Ab-Initio Total Energy Calculations for Metals and Semiconductors Using a Plane-Wave Basis Set. *Comput. Mater. Sci.* **1996**, *6*, 15–50.
- (50) Kresse, G.; Hafner, J. Ab Initio Molecular-Dynamics Simulation of the Liquid-Metal-Amorphous-Semiconductor Transition in Germanium. *Phys. Rev. B: Condens. Matter Mater. Phys.* **1994**, *49*, 14251.
- (51) Perdew, J. P.; Burke, K.; Ernzerhof, M. Generalized Gradient Approximation Made Simple. *Phys. Rev. Lett.* **1996**, *77*, 3865–3868.
- (52) Burke, K.; Ernzerhof, M.; Perdew, J. P. Generalized Gradient Approximation Made Simple. *Phys. Rev. Lett.* **1996**, *77*, 3865; *Phys. Rev. Lett.* **1997**, *78*, 1396.
- (53) Kresse, G.; Joubert, D. From Ultrasoft Pseudopotentials to the Projector Augmented-Wave Method. *Phys. Rev. B: Condens. Matter Mater. Phys.* **1999**, *59*, 1758.
- (54) Grimme, S. Semiempirical Gga-Type Density Functional Constructed with a Long-Range Dispersion Correction. *J. Comput. Chem.* **2006**, *27*, 1787–1799.
- (55) Dudarev, S. L.; Botton, G. A.; Savrasov, S. Y.; Humphreys, C. J.; Sutton, A. P. Electron-Energy-Loss Spectra and the Structural Stability of Nickel Oxide: An LSDA+ U Study. *Phys. Rev. B: Condens. Matter Mater. Phys.* **1998**, *57*, 1505.
- (56) Kramer, D.; Ceder, G. Tailoring the Morphology of LiCoO<sub>2</sub>: A First Principles Study. *Chem. Mater.* **2009**, *21*, 3799–3809.